UNIVERSITÄT AUGSBURG
Universitätsbibliothek

OPEN ACCESS
OPUS AUGSBURG

Coherence of turbulent structures with varying drive in stellarator edge plasmas

Paul Huslage, Gregor Birkenmeier, B. Shanahan, C. Killer

Angaben zur Veröffentlichung / Publication details:

Huslage, Paul, Gregor Birkenmeier, B. Shanahan, and C. Killer. 2024. "Coherence of turbulent structures with varying drive in stellarator edge plasmas." *Plasma Physics and Controlled Fusion* 66 (1): 015006. https://doi.org/10.1088/1361-6587/ad0ee5.

Nutzungsbedingungen / Terms of use:

CC BY 4.0

Dieses Dokument wird unter folgenden Bedingungen zur Verfügung gestellt: / This document is made available under these conditions:
CC-BY 4.0: Creative Commons: Namensnennung
Weitere Informationen finden Sie unter: / For more information see:
https://creativecommons.org/licenses/by/4.0/deed.de

Plasma Physics and
Controlled Fusion

PURPOSE-LED
PUBLISHING™

PAPER • OPEN ACCESS

Coherence of turbulent structures with varying drive in stellarator edge plasmas

To cite this article: P Huslage *et al* 2024 *Plasma Phys. Control. Fusion* **66** 015006

View the article online for updates and enhancements.

You may also like

- (Expected difficulties with) density-profile control in W7-X high-performance plasmas
C D Beidler, Y Feng, J Geiger et al.
- Development of a synthetic phase contrast imaging diagnostic for turbulence studies at Wendelstein 7-X
S K Hansen, M Porkolab, J-P Bähner et al.
- W7-X and the sawtooth instability: towards realistic simulations of current-driven magnetic reconnection
Alessandro Zocco, Alexey Mishchenko, Carolin Nührenberg et al.

This content was downloaded from IP address 137.250.100.44 on 09/11/2026 at 13:39

OPEN ACCESS
IOP Publishing
Plasma Physics and Controlled Fusion
Plasma Phys. Control. Fusion **66** (2024) 015006 (10pp)
https://doi.org/10.1088/1361-6587/ad0ee5

Coherence of turbulent structures with varying drive in stellarator edge plasmas

P Huslage[1,*], G Birkenmeier[1], B Shanahan[2] and C Killer[2]

[1] Max-Planck Institut für Plasmaphysik, Boltzmannstraße 2, Garching 85748, Germany
[2] Max-Planck Institut für Plasmaphysik, Wendelsteinstraße 1, Greifswald 17491, Germany

E-mail: paul.huslage@ipp.mpg.de

Received 5 July 2023, revised 7 November 2023
Accepted for publication 22 November 2023
Published 1 December 2023



Abstract

This work investigates the parallel coherence of plasma filaments through numerical simulations using the hot-ion two-fluid `hermes-2` model within the `BOUT++` framework. Realistic field lines in the scrape-off layer (SOL) of magnetic fusion devices, especially in stellarator configurations possess a highly varying curvature along the magnetic field line. A varying curvature creates a parallel $\mathbf{E} \times \mathbf{B}$ velocity gradient which might tear the filament apart. The main parameters controlling this process are the collisionality and the electron plasma beta. Simulations of realistic curvature variations along field lines in a circular ASDEX Upgrade-like tokamak and Wendelstein 7-X stellarator (W7-X) show the parallel displacement between different filament sections to correlate with the curvature. The rapidly varying W7-X curvature and the low average curvature drive reduce the propagation of the filament to only a few hundred meters per second. The effect of a finite ion temperature on filament propagation in a W7-X field line geometry is found to be a higher diamagnetic current resulting in stronger charge separation. This work supports simulations and experimental findings that filaments in W7-X are comparably slow due to the large major radius of the device. They do not perform ballistic motion and hence do not drive significant turbulence spreading in the SOL.

Keywords: turbulence, filaments, stellarator, W7-X, simulation

1. Introduction

Filaments are a well-known channel of particle and heat loss in the scrape-off layer (SOL) of tokamaks. A field-aligned monopole density perturbation leads to a dipole potential driving radial transport originating from the toroidal curvature of the field line [1]. Filaments propagate a distance several times their diameter transporting heat and particles from the edge into the SOL to drive turbulent dynamics in this region. This process is known as turbulence spreading and has been observed e.g. in the compact assembly (COMPASS) tokamak [2]. Measurements of blob densities and temperatures in tokamaks have been taken through various methods [3–6]. The database on turbulence in stellarators is comparatively small as there are fewer machines [7, 8]. The dipole polarization of a poloidal pressure perturbation is observed via a phase shift between floating potential and ion saturation current measurements in Wendelstein 7-AS (W7-AS) (proxies for plasma potential and density perturbations, respectively) [9]. Filamentary field-aligned structures which are connected to the sheath have been observed in the stellarators W7-AS and TJ-K [10–12]. In TJ-K blobs contribute as much as 30% of the total particle transport in the SOL and show a poloidal velocity component originating from a polarization due to the geodesic curvature [11]. Poloidal propagation has also been observed in W7-AS and in the large helical device (LHD) which is found to be triggered by a finite radial shear of the magnetic field [13, 14]. Experimental investigations with Langmuir probes found filamentary structures in Wendelstein 7-X (W7-X) to

* Author to whom any correspondence should be addressed.

Original Content from this work may be used under the terms of the Creative Commons Attribution 4.0 licence. Any further distribution of this work must maintain attribution to the author(s) and the title of the work, journal citation and DOI.

 © 2023 The Author(s). Published by IOP Publishing Ltd

propagate slowly in the radial direction due to the large major radius compared to ASDEX Upgrade (AUG) and therefore smaller curvature ($R_{\mathrm{maj}} = 6\,\mathrm{m}$ vs. 2.5 m with similar minor radius of 0.5 m). Scalings of the velocity with the perpendicular blob size show quantitative agreement with ion saturation current measurements of the midplane manipulator probe in W7-X despite neglecting the inhomogeneous curvature drive [15]. In contrast to axisymmetric tokamaks, stellarators such as W7-X feature a rapidly varying curvature drive along their field lines. In addition, W7-X uses an island divertor which introduces magnetic islands in the plasma edge that further add complexity due to strong gradients of magnetic shear (by having multiple X-points) and a complicated pattern of connection lengths to targets. The parallel connection length determines the magnitude of the parallel current and the propagation regime of the filament. Seeded blob simulations in an area with a sudden change of the parallel connection length suggest that blobs change their propagation regime provided they are still coherent enough by the time they propagate into the region of the abrupt change of the parallel connection length $L_{\parallel}$ [16]. The question of filament coherence for varying curvature has been tackled with cold filaments for pellet-relevant conditions [17]. Here, a non-uniform propagation of different parts of the filament at different positions along the field line is caused by such a curvature drive as can be found in W7-X. An increase in temperature is shown to lead to more coherent filaments. Parallel varying curvature, i.e. different magnitudes of the curvature drive at different locations of the field line, might explain why coherent structures decorrelate along a field line. The goal of this paper is to investigate the influence of non-uniform curvature along a magnetic field line on filament coherence and dynamics.

This work is structured as follows: section 2 introduces the `hermes-2` plasma model used in this work. Section 3 derives a quantitative measure to indicate whether a filament stays a coherent structure from Ohm's law, depending on the collisionality and the electron plasma beta. Section 4 contains the results of simulations of the influence of varying curvature drive on filaments for sinusoidal curvature. We use this simple curvature variation as a toy model to show the main physical mechanisms at play. Sections 5 and 6 present simulations with the curvature of a circular tokamak with AUG parameters and W-7X, respectively. This is done to study the effects found in section 4 in more realistic geometries and followed by a summary and discussion in section 7.

2. Numerical methods

The `hermes-2` model is the plasma two-fluid model used in this work. It is an extension of the `hermes` model factoring in effects of a finite, evolving ion temperature T_{i} [18, 19]. It uses the assumptions of a small β_{e}, magnetized, collisional plasma to simplify the Braginskii equations [20]. The resulting model equations evolve density n, electron pressure p_{e}, ion pressure p_{i}, parallel ion momentum $nv_{\parallel,\mathrm{i}}$, vorticity ω as well as the electrostatic potential ϕ and the parallel component of the vector potential ψ. The model also includes terms for interaction with neutral particles which are dropped in the following. Parallel derivatives are computed as $\nabla_{\parallel} f = (\nabla f \cdot \mathbf{b})\,\mathbf{b}$ and $\partial_{\parallel} f = \mathbf{b}\cdot\nabla f$. $\mathbf{b} = \mathbf{B}/B$ is the magnetic unit vector. Here, we give the `hermes-2` model equations:

$$\partial_t n = -\nabla\cdot(n\mathbf{v}_{\mathbf{E}} + n\mathbf{v}_{\mathrm{mag,e}}) - \nabla_{\parallel}\left(nv_{\parallel,\mathrm{e}}\right). \tag{1}$$

$\mathbf{v}_{\mathbf{E}} = \mathbf{E}\times\mathbf{B}/B^2$ denotes the $\mathbf{E}\times\mathbf{B}$ drift. Wherever possible, the diamagnetic drift $v_{\mathrm{dia},s} = \mathbf{b}\times\nabla p_s/q_s n B^2$ is replaced by the magnetic drift

$$\mathbf{v}_{\mathrm{mag},s} = -\frac{T_s}{q_s}\left(\nabla\times\frac{\mathbf{b}}{B}\right), \tag{2}$$

which is numerically advantageous [18]. It replaces the diamagnetic drift e.g. in the density equation, where the relevant divergence term is identical. T_s is the temperature of the species s.

$$\begin{aligned}\partial_t\omega = {}& \nabla\cdot\left((p_{\mathrm{e}}+p_{\mathrm{i}})\nabla\times\frac{\mathbf{b}}{B}\right) + \nabla_{\parallel} j_{\parallel} \\ & - \nabla\cdot\left(\frac{1}{2B^2}\nabla_{\perp}(\mathbf{v}_{\mathbf{E}}\cdot\nabla p_{\mathrm{i}}) + \frac{\omega}{2}\mathbf{v}_{\mathbf{E}}\right. \\ & \left. + \frac{n_0}{2B^2}\Delta_{\perp}\phi\,(\mathbf{v}_{\mathbf{E}} + \mathbf{v}_{\mathrm{dia,i}})\right) \\ & + \nabla\cdot\left(\frac{\pi_{\mathrm{ci}}}{2}\nabla\times\frac{\mathbf{b}}{B} - \frac{1}{3}\frac{\mathbf{b}\times\nabla\pi_{\mathrm{ci}}}{B}\right).\end{aligned} \tag{3}$$

The scalar gyroviscous stress tensor for ions is given by [19]

$$\begin{aligned}\pi_{\mathrm{ci}} = {}& \frac{3m_{\mathrm{i}}}{4p_{\mathrm{i}}T_{\mathrm{i}}}\left(0.20q_{\parallel,\mathrm{i}}^2 - 0.085q_{\mathrm{i}}^2\right) \\ & + 0.96\frac{p_{\mathrm{i}}}{\nu_{\mathrm{i}}}\kappa\cdot\left(\mathbf{v}_{\mathbf{E}} + \mathbf{v}_{\mathrm{dia,i}} + 1.61\frac{\mathbf{b}\times\nabla T_{\mathrm{i}}}{B}\right) \\ & - \frac{2}{\sqrt{B}}\partial_{\parallel}\left(\sqrt{B}v_{\parallel,\mathrm{i}}\right) - \frac{1.42}{p_{\mathrm{i}}\sqrt{B}}\partial_{\parallel}\left(\sqrt{B}q_{\parallel,\mathrm{i}}\right) \\ & - \frac{0.49q_{\parallel,\mathrm{i}}}{p_{\mathrm{i}}}\left(2.27\partial_{\parallel}\ln T_{\mathrm{i}} - \partial_{\parallel}\ln p_{\mathrm{i}}\right).\end{aligned} \tag{4}$$

The vorticity is simplified via the boussinesq approximation which replaces the density with a constant value n_0 assuming density fluctuations to be much smaller than potential fluctuations so that $\nabla\cdot(n\partial_t\nabla_{\perp}\phi) \approx n_0\partial_t\nabla_{\perp}^2\phi$ [21]. The vorticity reads

$$\omega = \nabla\cdot\left(\frac{1}{B^2}\left(n_0\nabla_{\perp}\phi + \nabla_{\perp}p_{\mathrm{i}}\right)\right). \tag{5}$$

The numerical prefactors in the ion gyroviscous stress tensor are derived by Braginskii [22]. The closures of this system are given by the parallel and total ion heat fluxes [19]

$$q_{\parallel,\mathrm{i}} = -\kappa_{\parallel,\mathrm{i}}\partial_{\parallel}T_{\mathrm{i}}, \tag{6}$$

$$q_{\mathrm{i}}^2 = \left(\kappa_{\parallel,\mathrm{i}}^2 - \left(\frac{5}{2}p_{\mathrm{i}}\right)^2\right)\left(\partial_{\parallel}T_{\mathrm{i}}\right)^2 + \left(\frac{5}{2}p_{\mathrm{i}}\nabla T_{\mathrm{i}}\right)^2.$$

These expressions are the Spitzer–Harm heat fluxes used in the popular transport code `SOLPS` [23].

$$\begin{aligned}\frac{3}{2}\partial_t p_\mathrm{e} = &-\nabla\cdot\left(\frac{3}{2}p_\mathrm{e}\mathbf{v}_\mathbf{E}+\frac{5}{2}p_\mathrm{e}\mathbf{v}_{\mathrm{mag,e}}\right)-p_\mathrm{e}\nabla\cdot\mathbf{v}_\mathbf{E}\\&-\nabla\cdot\left(\frac{3}{2}p_\mathrm{e}v_{\parallel,\mathrm{e}}\right)-p_\mathrm{e}\nabla_\parallel v_{\parallel,\mathrm{e}}+\nabla_\parallel\left(\kappa_{\parallel,\mathrm{e}}\partial_\parallel T_\mathrm{e}\right)\\&+0.71\nabla_\parallel\left(T_\mathrm{e}j_\parallel\right)-0.71j_\parallel\partial_\parallel T_\mathrm{e}+\frac{\nu}{n}j_\parallel^2\\&+\nabla\cdot\left(\frac{\rho_\mathrm{e}^2}{t_\mathrm{e}}\left(\nabla_\perp p_\mathrm{e}+\nabla_\perp p_\mathrm{i}+\frac{11}{12}n\nabla_\perp T_\mathrm{e}\right)\right).\end{aligned}\tag{7}$$

$$\begin{aligned}\frac{3}{2}\partial_t p_\mathrm{i} = &-\nabla\cdot\left(\frac{3}{2}p_\mathrm{i}\mathbf{v}_\mathbf{E}+\frac{5}{2}p_\mathrm{i}\mathbf{v}_{\mathrm{mag,i}}\right)-p_\mathrm{i}\nabla\cdot\mathbf{v}_\mathbf{E}\\&-\nabla\cdot\left(\frac{3}{2}p_\mathrm{i}\mathbf{b}v_{\parallel,\mathrm{i}}\right)-p_\mathrm{i}\nabla_\parallel v_{\parallel,\mathrm{i}}-\frac{j_\parallel}{n_0}\partial_\parallel p_\mathrm{i}\\&+\frac{p_\mathrm{i}}{n_0}\nabla\cdot\left(\left(p_\mathrm{e}+p_\mathrm{i}\right)\nabla\times\frac{\mathbf{b}}{B}\right)+v_{\parallel,\mathrm{i}}\frac{2}{3}B^{\frac{3}{2}}\partial_\parallel\left(\frac{\pi_\mathrm{ci}}{B^{3/2}}\right)\\&+\nabla_\parallel\left(\kappa_{\parallel,\mathrm{i}}\partial_\parallel T_\mathrm{i}\right)+\nabla\cdot\left(\kappa_{\perp,\mathrm{i}}\nabla_\perp T_\mathrm{i}\right)\\&+\frac{5}{2}\nabla\cdot\left(\frac{T_\mathrm{i}\rho_\mathrm{e}^2}{T_\mathrm{e}t_\mathrm{e}}\left(\nabla_\perp p_\mathrm{e}+\nabla_\perp p_\mathrm{i}-\frac{3}{2}n\nabla_\perp T_\mathrm{e}\right)\right)\\&-\frac{3T_\mathrm{i}}{10t_\mathrm{i}B^2}\nabla_\perp\omega\cdot\nabla\left(\phi+\frac{p_\mathrm{i}}{n_0}\right)\\&-\left(\frac{\pi_\mathrm{ci}}{2}\nabla\times\frac{\mathbf{b}}{B}-\frac{1}{3}\frac{\mathbf{b}\times\nabla\pi_\mathrm{ci}}{B}\right)\cdot\nabla\left(\phi+\frac{p_\mathrm{i}}{n_0}\right).\end{aligned}\tag{8}$$

The parallel and perpendicular ion heat conduction coefficients are given by

$$\kappa_{\parallel,\mathrm{i}}=3.9\frac{p_\mathrm{i}t_\mathrm{i}}{m_\mathrm{i}}\quad\kappa_{\perp,\mathrm{i}}=2\frac{n\rho_\mathrm{i}^2}{t_\mathrm{i}}.\tag{9}$$

Here, t_e and t_i are the electron and ion collision times.

$$\begin{aligned}\partial_t\left(nv_{\parallel,\mathrm{i}}\right) = &-\nabla\cdot\left(nv_{\parallel,\mathrm{i}}\left(\mathbf{v}_\mathbf{E}+\mathbf{b}v_{\parallel,\mathrm{i}}+\mathbf{v}_{\mathrm{mag,i}}\right)\right)\\&-\partial_\parallel p_\mathrm{e}-\partial_\parallel p_\mathrm{i}-\frac{2}{3}B^{\frac{3}{2}}\partial_\parallel\left(\frac{\pi_\mathrm{ci}}{B^{3/2}}\right)\\&+\nabla\cdot\left(v_{\parallel,\mathrm{i}}\frac{\rho_\mathrm{e}^2}{t_\mathrm{e}T_\mathrm{e}}\left(\left(T_\mathrm{e}+T_\mathrm{i}\right)\nabla_\perp n\right.\right.\\&\left.\left.+\,n\left(\nabla_\perp T_\mathrm{i}-\frac{1}{2}\nabla_\perp T_\mathrm{e}\right)\right)\right).\end{aligned}\tag{10}$$

$$\begin{aligned}\partial_t\left(\frac{m_\mathrm{e}}{m_\mathrm{i}}\left(v_{\parallel,\mathrm{e}}-v_{\parallel,\mathrm{i}}\right)+\frac{1}{2}\beta_\mathrm{e}\psi\right) = &\partial_\parallel\phi-\frac{1}{n}\partial_\parallel p_\mathrm{e}-0.71\partial_\parallel T_\mathrm{e}\\&+\frac{\nu j_\parallel}{n}+\frac{m_\mathrm{e}}{m_\mathrm{i}}\left(\mathbf{v}_\mathbf{E}+\mathbf{b}v_{\parallel,\mathrm{i}}\right)\\&\cdot\nabla\left(v_{\parallel,\mathrm{i}}-v_{\parallel,\mathrm{e}}\right).\end{aligned}\tag{11}$$

Here, β_e is the electron plasma beta, whereas ν is the collisionality. The `hermes-2` model conserves the particle number $N=\int \mathrm{d}V n$ and an energy E

$$\begin{aligned}E = &\int \mathrm{d}V\frac{m_\mathrm{i}n_0}{2}\left|\frac{\nabla_\perp\phi}{B}+\frac{\nabla_\perp p_\mathrm{i}}{en_0B}\right|^2+\frac{1}{2}m_\mathrm{i}nv_{\parallel,\mathrm{i}}^2\\&+\frac{3}{2}\left(p_\mathrm{i}+p_\mathrm{e}\right)+\frac{1}{4}\beta_\mathrm{e}\left|\nabla\psi\right|^2+\frac{m_\mathrm{i}}{2m_\mathrm{e}}\frac{j_\parallel}{n}.\end{aligned}\tag{12}$$

`hermes-2` contains self-consistent expressions for classical diffusion in the equations for density, vorticity, electron and ion pressure as well as parallel momentum. This avoids the introduction of unphysical, numerical diffusion coefficients [24]. These terms are motivated by a classical random walk ansatz for the particle motion perpendicular to the magnetic field. The typical increment is the Larmor radius $\rho_s = q_sB/m_s$. Simulations are performed in a curved slab geometry. We assume zero magnetic shear so that the curvature does not vary perpendicular to the magnetic field. The coordinate system is spanned by the radial, parallel, and binormal direction (x,y,z), respectively. The resolution (n_x,n_y,n_z) is (132, 16, 128). The size of the simulation domain is $(L_x,L_y,L_z)=(L_\perp,L_\parallel,L_\perp)$. The perpendicular domain width $L_\perp$ is chosen between 0.1 m and 0.15 m to encompass the filament with sufficient distance to the boundary. The parallel domain length is equal to the parallel connection length $L_\parallel$. The domain is designed to have a sinusoidal curvature variation along the parallel direction. This determines the curvature scale length $L_\kappa = L_\parallel/2$. The filament is initialized as a Gaussian density perturbation in the perpendicular direction and homogeneously along the field line. Its position and velocity are obtained by calculating its center of mass at the poloidal plane at each of the n_y parallel grid points. Temperatures and the density in the model equations are normalized to reference values T and n_0, respectively. In `hermes-2` varying these is also used to change the collisionality and the electron plasma beta. The relative amplitude of the initial density perturbation and the electron pressure amplitude are 100% above the background. The ion pressure perturbation is three times the electron pressure perturbation to account for hot ions inspired by experimental results [3]. Collisional energy exchange is turned off to keep the background temperatures flat.

3. Parallel displacement

The propagation of filaments is induced by $\mathbf{E}\times\mathbf{B}$ advection. It is caused by a charge separation resulting from a finite divergence of the diamagnetic current. This takes place due to a finite magnetic field curvature [25, 26].

$$\begin{aligned}\nabla\cdot\mathbf{j}_\mathrm{dia} &= \nabla\cdot\left(\frac{\mathbf{b}\times\nabla p}{B}\right)=\left(\nabla\times\frac{\mathbf{b}}{B}\right)\cdot\nabla p\\&=\left(\frac{1}{B}\mathbf{b}\times\kappa+\frac{1}{B^2}\mathbf{b}\times\nabla B\right)\cdot\nabla p.\end{aligned}\tag{13}$$

where $\kappa=\mathbf{b}\cdot\nabla\mathbf{b}=\mathbf{b}\times(\nabla\times\mathbf{b})$ is the magnetic curvature. A pressure gradient parallel to $\mathbf{b}\times\kappa$ or $\mathbf{b}\times\nabla B$ leads to a charge accumulation due to a finite divergence of the perpendicular current. A magnetic field gradient is linked to the curvature via [27]

$$\kappa = \mathbf{b} \times \left(\nabla \times \frac{\mathbf{B}}{B} \right) = -\mathbf{b} \times \frac{\mu_0 \mathbf{j} + \mathbf{b} \times \nabla B}{B} = \frac{\mu_0 \nabla p}{B^2} + \frac{\nabla_\perp B}{B}. \tag{14}$$

For a low-β plasma, the pressure contribution in the above formula can be neglected and we can replace the ∇B term, resulting in

$$\nabla \cdot \mathbf{j}_{\text{dia}} = \frac{2\nabla p}{B} (\mathbf{b} \times \kappa). \tag{15}$$

The curvature of a magnetic field line can be split up into its normal and geodesic components. The normal curvature κ_n quantifies to which extent the curvature vector is normal to the flux surface

$$\kappa_\text{n} = \mathbf{n} \cdot \kappa. \tag{16}$$

The vector $\mathbf{n}$ is the normal vector of the flux surface. The geodesic curvature κ_g describes the part of the curvature tangential to the flux surface

$$\kappa_\text{g} = (\mathbf{n} \times \mathbf{b}) \cdot \kappa. \tag{17}$$

If the magnitude of the curvature drive varies along the field line, the charge separation becomes inhomogeneous. Different regions along the field line exhibit different levels of charge accumulation. A parallel potential gradient $\partial_\parallel \phi$ arises. This leads to differential $\mathbf{E} \times \mathbf{B}$ advection at different positions of the filament along the field line. The parallel current $j_\parallel$ sets in to flatten the potential gradient. The propagation time of the parallel current is limited by collisional/ohmic resistance and inductance. These are controlled by the collisionality ν and the electron plasma beta β_e, respectively.

This leaves two competing timescales. If the parallel current resolves the potential gradient fast enough the filament stays a coherent structure. Otherwise, the filament rips apart due to differential $\mathbf{E} \times \mathbf{B}$ advection. The perpendicular displacement Δ of a filament between the points of highest curvature (y_max) and lowest curvature (y_min) after one blob coherence time τ_B is chosen as a measure for parallel coherence. To indicate whether a filament stays together as a connected structure along the field line, Δ is defined as the perpendicular distance between the centers of mass $\mathbf{r}(y) = (x, z)$ in the respective poloidal plane

$$\Delta = \left(\left(x(\tau_b, y_\text{min}) - x(\tau_b, y_\text{max}) \right)^2 + \left(z(\tau_b, y_\text{min}) - z(\tau_b, y_\text{max}) \right)^2 \right)^{\frac{1}{2}}. \tag{18}$$

For later use, the radial and binormal displacements are also defined:

$$\Delta_x/\delta_\perp = x(\tau_b, y_\text{min}) - x(\tau_b, y_\text{max})$$
$$\Delta_z/\delta_\perp = z(\tau_b, y_\text{min}) - z(\tau_b, y_\text{max})$$

Displacement is illustrated in figure 1. The advection is assumed to happen on the advection timescale $\tau_B = \delta_\perp / v_b$ for a filament of perpendicular size $\delta_\perp$ and characteristic velocity v_b. This is the timescale in which a blob travels a distance of $\delta_\perp$. Parallel Ohm's law (equation (11)) in the `hermes-2` model used in the following sections rearranged for the parallel potential gradient reads

$$\partial_\parallel \phi = \frac{1}{2} \beta_\text{e} \partial_t \psi + \frac{1}{n} \partial_\parallel p_\text{e} + 0.71 \partial_\parallel T_\text{e} + \frac{\nu j_\parallel}{n}. \tag{19}$$

The above equation (19) is connected to the parallel gradient of the perpendicular blob velocity via $\partial_\parallel \phi = B \delta_\perp \partial_\parallel v_b$. Inserting parallel Ampere's law ($j_\parallel = -\nabla_\perp^2 \psi \sim -\delta_\perp^{-2} \psi$), integrating the above equation (19) and rewriting it in characteristic blob quantities with the blob correspondence principle [1, 25] gives an expression for the parallel displacement between the part of highest and lowest curvature

$$\int_0^{\tau_b} \mathrm{d}t \, \partial_\parallel \phi \sim \delta_\perp \int_0^{\tau_b} \mathrm{d}t \, \partial_\parallel v_b := \frac{\Delta \delta_\perp}{L_\kappa}, \tag{20}$$

$$\Delta/\delta_\perp \sim -\left(\frac{\beta_\text{e} L_\kappa}{2} + \frac{\nu L_\kappa \tau_b}{n \delta_\perp^2} \right) j_\parallel + \frac{\tau_b}{n \delta_\perp^2} p_\text{e} + 0.71 \frac{\tau_b}{\delta_\perp^2} T_\text{e}. \tag{21}$$

We assume that the parallel derivatives scale as the curvature scale length ($\partial_\parallel \sim L_\kappa^{-1}$). The displacement Δ is normalized to the perpendicular blob size $\delta_\perp$. A filament is considered coherent for $\Delta/\delta_\perp < 1$. The parallel gradients are expected to scale with the length of the parallel curvature features L_κ. Discarding the parallel temperature and pressure gradients gives a scaling for the displacement depending on normalized collisionality ν' and electron plasma beta β'_e normalized to the blob size

$$\Delta/\delta_\perp \sim \left(\frac{\beta_\text{e} L_\kappa}{2} + \frac{\nu L_\kappa \tau_b}{n \delta_\perp^2} \right) j_\parallel := (\beta' + \nu') j_\parallel. \tag{22}$$

It becomes clear from this equation that a higher electron plasma beta and a higher collisionality lead to a higher displacement between the different parts of the filament subject to different curvature drives.

4. Simulations with sinusoidal curvature drive

The normal curvature in a toroidal magnetic field with a finite rotational transform follows roughly a sinusoidal pattern. This is further illustrated in the later sections (a comparison between the curvature for two stellarators and a tokamak can also be found in [28]). Here, we consider a simple, sinusoidal curvature drive

$$(\mathbf{b} \times \kappa) = 0.6 \sin(y) \hat{\mathbf{x}}. \tag{23}$$

It corresponds to the normal curvature of an infinite aspect ratio tokamak (see equation (26)) and serves as a toy problem to understand the relationship between filament coherence

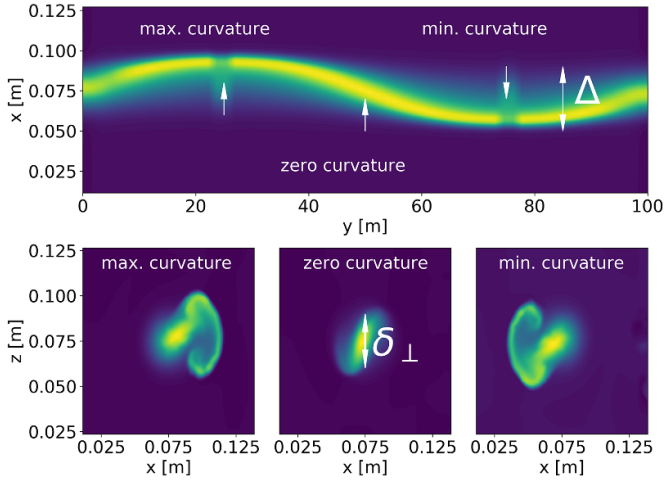

Figure 1. A filament subject to sinusoidal curvature drive along the magnetic field line. The blob propagates in different directions at different parallel positions. The blob shows the typical mushroom shape [1] at the maximum/minimum of the drive while the filament structure at zero curvature does not propagate perpendicularly. It spreads along the field line as it is disconnected from the advecting parts.

and varying curvature. A parallel varying curvature leads to an inhomogeneous filament drive due to varying divergence of the diamagnetic current. The response of the parallel current depends on the ohmic and inductive resistance parallel to the magnetic field.

Figure 1 shows the parallel displacement of a filament with a sinusoidal curvature profile along the field line. The displacement follows the curvature, i.e. in regions of strong curvature the displacement is largest and the direction of filament propagation depends on the sign of the curvature. In this case ($n = 10^{19}\,\mathrm{m}^{-3}$, $T = 100\,\mathrm{eV}$) the parallel ohmic and inductive resistance is large enough to hinder the parallel current sufficiently. The filament propagates in different directions at the position of minimal and maximal curvature. The advecting parts of the filament develop a mushroom-shaped Kelvin–Helmholtz instability. The part of the filament at the center of the parallel domain stands still in the perpendicular direction and spreads out along the field line as a parallel pressure gradient arises due to the differential advection.

The effects of ohmic and inductive resistance are first illustrated separately. According to equation (22) a larger normalized electron plasma beta β_e' or collisionality ν' increase the normalized parallel displacement $\Delta/\delta_\perp$.

For electrostatic simulations ($\beta_\mathrm{e} = 0$) the parallel current is only limited by the collisionality ν. At constant temperature $T = 10\,\mathrm{eV}$ simulations with varying densities from $10^{18}\,\mathrm{m}^{-3}$ to $10^{19}\,\mathrm{m}^{-3}$ and $L_\parallel$ from 10 m to 200 m are performed. These are visible in figure 2(top). The displacement first increases for higher normalized collisionality as expected from equation (22). It then saturates and becomes independent of ν' for larger collisionalities as the blob dynamics is fully determined by perpendicular effects and parallel currents do not have a significant influence anymore.

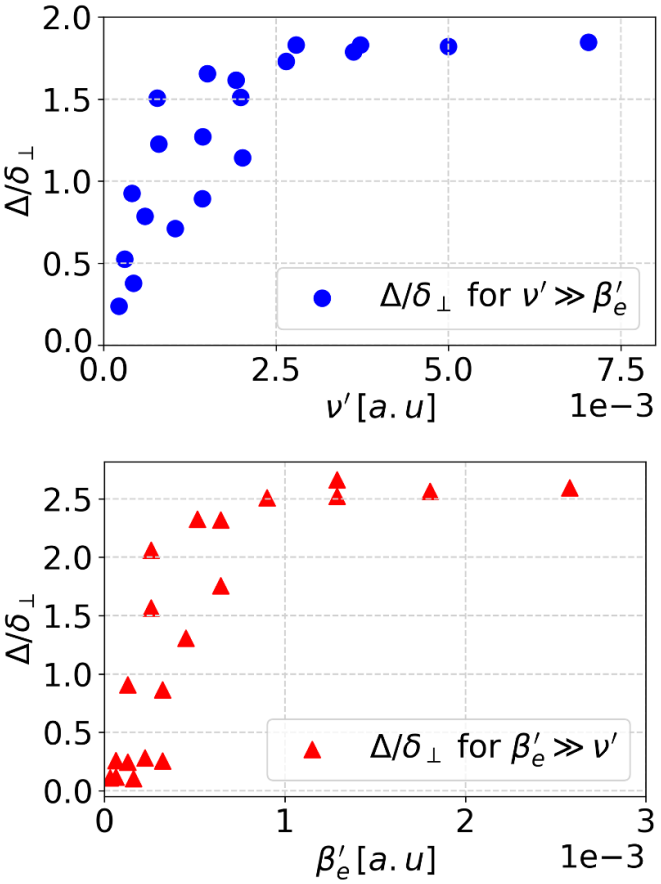

Figure 2. Normalized displacement of filaments subject to a sinusoidal curvature for collisionally (top) and electromagnetically (bottom) dominated regimes. The displacement increases as the parallel current is limited by ohmic resistance or inductance thus disconnecting parallel separate regions. For large β_e' or ν', the parallel current does not have any influence on the advection timescale. The displacement does not further increase. Different saturation levels are due to the different absolute blob sizes. The blob size is kept at $40\rho_\mathrm{i}$, and the ion Larmor radius changes.

A similar picture appears for simulations with high β_e' and low ν' in figure 2(bottom). Here, the temperature is set to $T = 100\,\mathrm{eV}$. The densities and parallel connection lengths from the collisionality scan are kept the same. The parallel current is primarily limited by the inductance. At sufficiently high β_e' the parallel current is entirely damped on the advection timescale. A further increase in β_e' does not influence the perpendicular blob dynamics and hence a saturation of $\Delta/\delta_\perp$ with β_e as shown in figure 2 takes place.

Equation (22) discards the pressure term in parallel Ohm's law (19). A parallel pressure gradient drives a parallel flow. The influence of the $\partial_\parallel p_\mathrm{e}$ (and $\partial_\parallel T_\mathrm{e}$) contribution is larger compared to the collisionality and electromagnetic terms for lower connection lengths as both expressions of β_e' and ν' scale linearly with $L_\parallel$ and $\partial_\parallel p_\mathrm{e}$ scales as $p_\mathrm{e}/L_\parallel$. Simulations with similar normalized collisionality ν' or β_e' show higher displacement for longer $L_\parallel$. This explains the scattering of the displacement values in figure 2.

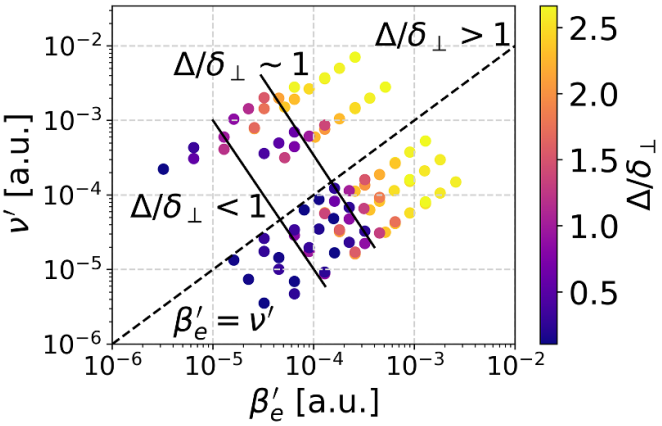

Figure 3. Normalized displacement of filaments for a sinusoidal curvature drive in (β'_e, ν') space for temperatures from 10 eV to 100 eV and densities from $10^{18}\,\mathrm{m}^{-3}$ to $10^{19}\,\mathrm{m}^{-3}$. The displacement is largest for large $\beta'_e + \nu'$.

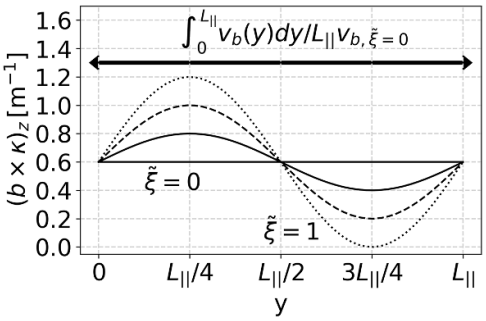

Figure 4. Curvature profiles for the simulations shown in figure 5. ξ_0 is fixed at $0.6\,\mathrm{m}^{-1}$ while $\tilde{\xi}$ varies. The averaged velocity of the filament along the field line is taken for figure 5.

The different saturation levels in figure 2 can be understood from the velocity scalings. The temperature is 10 eV in the collisionally dominated regime and 100 eV in the electromagnetically dominated regime. The blob used in these simulations has an initial size of $40\rho_\mathrm{i}$. Due to the high collisionality or electron plasma beta, the blob propagates in the inertial regime, so $v_b \sim \delta^{1/2}$ [1]. The Larmor radius scales with the square root of the temperature, therefore $v_b \sim (40\rho_i)^{1/2} \sim T^{1/4}$ and the ratio between the displacements which scale with the velocity according to equation (20) is expected to be equal. Indeed, the ratio of the two blob velocities is $10^{1/4} \approx 1.7$. The ratio of the saturation levels between the β'_e and ν' dominated simulations is approximately $2.5/1.8 \approx 1.4$ and lies in a similar range.

The influence of the two main control parameters β'_e and ν' has been examined separately in the previous section. Both effects can be combined to cover the parameter space relevant to filamentary transport in toroidal fusion devices.

The parameter scan behind figure 3 covers densities from $10^{18}\,\mathrm{m}^{-3}$ to $10^{19}\,\mathrm{m}^{-3}$, temperatures from 10 eV to 100 eV and parallel connection lengths from 25 m to 200 m. This leads to a two-dimensional evaluation of the parallel coherence of turbulent structures for a relevant $(\beta'_\mathrm{e}, \nu')$ space. The displacement between the maximum and minimum of the normal curvature increases from the bottom left to the top right. High $(\beta'_\mathrm{e}, \nu')$ lead to significant displacements larger than the initial blob size $\delta_\perp$. The parallel current is not able to flatten the parallel potential gradient $\partial_\parallel \phi$ within the advection timescale.

The simulations can be classified in two ways: they differ in their displacement as color-coded in figure 3. Incoherent blobs reach $\Delta > \delta_\perp$ meaning that the filament is ripped apart within one advection time τ_b. For coherent filaments, the normalized displacement stays below unity. In a coherent blob, the differential advection is not able to displace the different parallel parts of the filament by more than one perpendicular blob size $\delta_\perp$ relative to each other within one blob coherence time. The other distinction is between the dominant limiting factor of the parallel current. It is either bound by collisional or electromagnetic effects. In figure 3 these different regimes are indicated by a dashed $(\beta'_\mathrm{e} = \nu')$ line and two lines perpendicular to the former indicating $\Delta < \delta_\perp$ and $\Delta > \delta_\perp$. The influence of the pressure term leads to simulations in which very similar $(\beta'_\mathrm{e}, \nu')$ show different displacements depending on the parallel connection length. Higher $L_\parallel$ cause higher displacements. The pressure gradient $\partial_\parallel p_\mathrm{e}$ drives a parallel flow that acts against the ohmic and inductive terms. It flattens the parallel pressure gradient and scales as $1/L_\parallel$. The pressure-driven flows decrease for an increase in the parallel connection length. The local curvature drive [29] in the following simulations is the sum of the average drive ξ_0 and a sinusoidal variation with amplitude $\tilde{\xi}$ so that

$$(\mathbf{b} \times \kappa) = \left(\xi_0 + \tilde{\xi}\sin(y)\right)\hat{\mathbf{z}}. \tag{24}$$

In the following simulations $\xi_0 = 0.6\,\mathrm{m}^{-1}$ is chosen as $1/R_\mathrm{maj}$ of AUG. Figure 4 shows several curvature profiles with varying $\tilde{\xi}$. Figure 5 shows the maximum averaged velocity of a filament of size $\delta_\perp = 30\rho_\mathrm{i}$ against the relative curvature variation $\tilde{\xi}/\xi_0$.

For $\tilde{\xi}/\xi_0 > 1$, the curvature variation leads to a significant deceleration of the filament compared to the unperturbed case. This effect is increased for larger contributions of inductance and resistance $(\beta'_\mathrm{e}, \nu')$. In figure 5 the effect of the varying curvature is much stronger for $n = 10^{19}\,\mathrm{m}^{-3}$, $T = 100\,\mathrm{eV}$ (corresponding $\nu' = 8.1 \cdot 10^{-5}, \beta'_\mathrm{e} = 1.3 \cdot 10^{-3}$) compared to $n = 10^{18}\,\mathrm{m}^{-3}$, $T = 10\,\mathrm{eV}$ (corresponding to $\nu' = 4.1 \cdot 10^{-4}, \beta'_\mathrm{e} = 1.3 \cdot 10^{-5}$). The sum $\nu' + \beta'_\mathrm{e}$ in this plot increases from red to blue to green. In the most extreme case, the velocity is less than a quarter compared to the unperturbed case.

The deceleration of the filament compared to constant curvature is caused by the parallel flows driven by $\partial_\parallel p_\mathrm{e}$. They decrease the amplitude of the perpendicular pressure perturbation and therefore the filament drive. For $\tilde{\xi}/\xi_0 \geqslant 1$ this contribution of the varying curvature to the filament velocity becomes dominant over the average curvature drive leading to significant displacements. The filament loses parallel coherence. The small increase in velocity for $\tilde{\xi}/\xi_0 < 1$ compared to

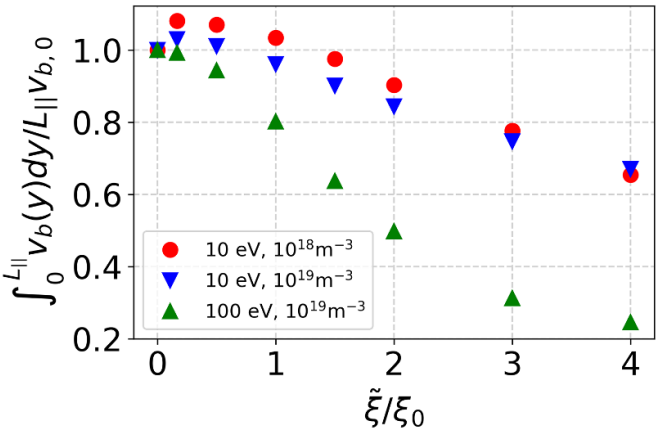

Figure 5. Toroidally averaged velocities for filaments with an average curvature drive plus a sinusoidal perturbation. For large perturbation amplitudes, the averaged filament velocity decreases significantly for higher β_e' or ν'.

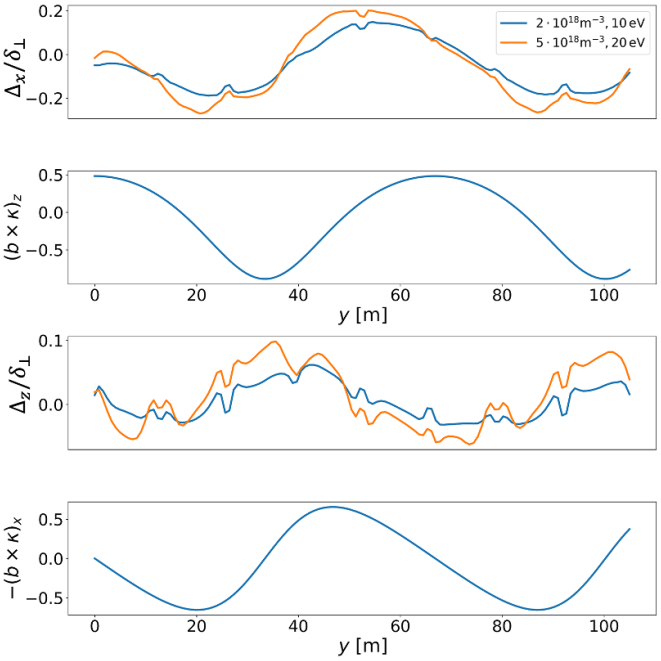

Figure 6. Radial and binormal displacement of a filament in a circular tokamak with AUG-like parameters. The displacement correlates with the respective components of the $\mathbf{b}\times\kappa$ vector which drives the charge separation. The simulation with higher $(\nu'+\beta_e')$ shows a higher displacement $\Delta/\delta_\perp$.

the simulation with no variation can be attributed to the influence of the sheath boundary condition on the center of mass calculation. It influences parts of the blob farther away from the boundary at $y=0$ and $y=L_\parallel$ for the 10 eV cases.

5. Simulations of a field line in a circular tokamak

In this section, the results of simulations with the curvature profile of a circular tokamak are shown. Its magnetic field reads [30]

$$\mathbf{B} = B_0\left(0, 1-\frac{r}{R_0}\cos(\theta), \frac{r}{qR_0}\left(1-\frac{r}{R_0}\cos(\theta)\right)\right)^{\mathrm{T}}. \quad (25)$$

From that the curvature vector $(\mathbf{b}\cdot\nabla\mathbf{b})$ can be calculated. The corresponding expressions for normal and geodesic curvature read

$$\kappa_n = -\frac{1}{1+\left(\frac{r}{qR_0}\right)^2}\left(\frac{r}{q^2R_0^2}+\frac{\cos(\theta)}{R_0+r\cos(\theta)}\right)$$
$$\kappa_g = \frac{1}{\sqrt{1+\left(\frac{r}{qR_0}\right)^2}}\frac{\sin(\theta)}{R_0+r\cos(\theta)}. \quad (26)$$

With AUG-like parameters ($R_0=1.6$ m, $r=0.5$ m, $q=4$) the blob temperatures and densities are taken from measurements in AUG L-Mode plasmas [3]. The simulation domain has the dimensions $L_\perp=0.15$ m and $L_\parallel=100$ m. The resolution is $132\times64\times128$.

Figure 6 shows the displacement in radial and binormal directions. The radial displacement correlates with the binormal component of the curvature drive term $(\mathbf{b}\times\kappa)_z=-\kappa_n$. The radial component of this vector is similar to the geodesic curvature and correlates with the binormal displacement.

The local curvature drives the charge separation which leads to differential $\mathbf{E}\times\mathbf{B}$ advection. The difference in displacement is increased for a higher ion temperature as this increases the curvature drive. For AUG-like parameters, the displacement stays smaller than the perpendicular blob size. The parallel current resolves the potential too fast to create significant displacement. This can be understood from the displacement scaling in equation (22). The AUG-like parameters (10 eV, 10^{18} m^{-3}) correspond to the lower end of the (β_e', ν') parameter space spanned in figure 3. The temperature and density are comparatively low while the curvature fall-off length is similar to the sinusoidal curvature used during section 4 with $L_\parallel=100$ m. The displacement of the equivalent data point in figure 3 is $\Delta/\delta_\perp=0.79$. This is higher than the displacement observed in this simulation ($\Delta/\delta_\perp=0.34$), which can be explained by the lower density and pressure perturbations compared to the previous section. The low displacement observed for AUG-like parameters in a circular tokamak is compatible with the parameter dependencies found for sinusoidal curvature.

For higher density and temperature ($5\cdot10^{18}$ m^{-3}, 50 eV) a higher normalized displacement of 0.47 is found, which compares similarly to the analogous displacement from figure 3 of 1.27.

6. Simulations of a W7-X field line

The divertor structure of W7-X utilizes islands in the magnetic field. This region experiences a strong variation in the parallel connection length as well as a highly inhomogeneous curvature. In the next operation phase of W7-X, there will be a gas puff imaging diagnostic installed to investigate the plasma

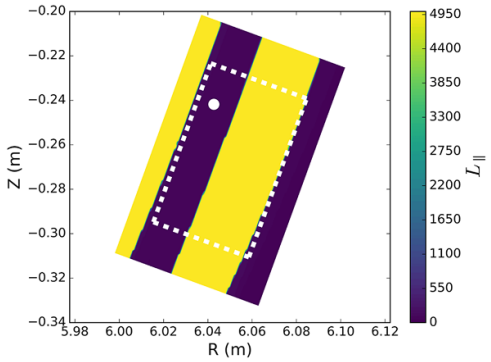

Figure 7. The field of view of the GPI diagnostic with the $L_\parallel$ profile [16]. The white dot indicates the position where the field line used in this section crosses the plane of sight. The island divertor creates regions of closed field lines (yellow) outwards of the primary separatrix.

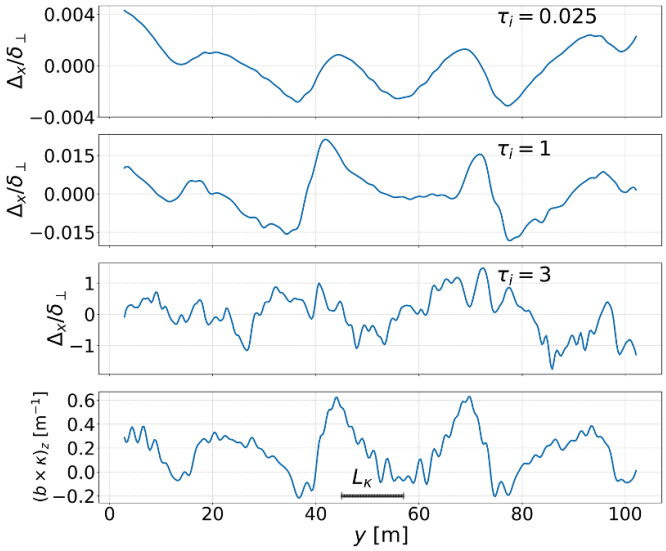

Figure 8. Radial displacement of a filament along a field line at the observation point of the new GPI diagnostic and the binormal component of the $\mathbf{b} \times \kappa$ vector. The curvature fall-off length L_κ of the most prominent curvature feature is indicated. The displacement follows the curvature. It increases with an increased amplitude of the ion pressure perturbation which increases the drive.

edge near a magnetic island [31]. The field of view of the diagnostic is displayed in figure 7.

Effects of a sharp transition in $L_\parallel$ have been investigated in [29]. The following simulations feature the realistic curvature profile of a W7-X field line crossing the line of sight of this diagnostic.

Simulations are performed in which a filament is initialized as a Gaussian pressure perturbation in the perpendicular directions and homogeneous along a field line. The curvature profile of the W7-X field line is taken from the IPP-Webservices [32]. The curvature is calculated using a field line tracer.

The information about blob size and density is taken from recent experimental studies [15]. The filament is initialized with $\delta_\perp \approx 1\,\mathrm{cm}$, a background density of $6 \cdot 10^{18}\,\mathrm{m}^{-3}$ and a density perturbation of 30% above the background. The electron temperature is 22 eV with a 10% perturbation. $\tau_\mathrm{i} = T_\mathrm{i}/T_\mathrm{e}$ is the ratio of ion and electron temperature. Filaments in [15] were assumed to have a flat T_i profile. Therefore, three different cases are investigated: a cold ion case with $\tau_\mathrm{i} = 0.025$, a case with equal electron and ion temperature ($\tau_\mathrm{i} = 1$), and a hot ion case ($\tau_\mathrm{i} = 3$). The relative ion temperature fluctuation amplitude is set to 10%.

The perpendicular displacement along the field line correlates with the curvature which can be seen in figure 8. This is similar to the simulations of circular tokamak curvature in the previous section. For the cold-ion case, the radial displacement strongly follows the curvature profile. All large-scale curvature features are represented in the radial displacement. This correlation becomes weaker for higher ion temperatures. A strong ion pressure perturbation creates a monopole contribution to the potential via the ion polarization current. A monopole potential structure leads to a rotary $\mathbf{E} \times \mathbf{B}$ motion which leads to a share of the advection being in the binormal direction. The simulations with $\tau_\mathrm{i} = 0.025$ and 1 show very little displacement on the order of 0.01. For the hot ion case, the displacement at the most prominent curvature feature exceeds one blob size. The displacement is enhanced for higher τ_i as this increases the overall pressure perturbation and the curvature drive.

The displacement of the most similar data point ($5 \cdot 10^{18}, 20\,\mathrm{eV}$) with sinusoidal curvature is $\Delta/\delta_\perp = 2.12$. This is much higher compared to the W7-X simulations with $\tau_\mathrm{i} = 3$. This can be once again understood from the scaling: the displacement in formula 22 scales linearly with the curvature fall-off length which is much shorter for the W7-X field line compared to the sinusoidal case. It shows a rippling of the curvature profile. As the parallel connection length is 105 m the curvature fall of length is approximately 10 m. The simulations in section 4 are performed on a sinusoidal curvature with only one period along the field line. The curvature fall-off length is $L_\parallel/2 = 50\,\mathrm{m}$. Additionally, the density and temperature perturbations are smaller. The density perturbation is only 30% compared to 100% in the previous simulations. The drive of the filaments is reduced compared to the previous simulations.

The simulations $\tau_\mathrm{i} = 0.025$, 1 and 3 show propagation speeds of around $100\,\mathrm{m\,s^{-1}}$, $200\,\mathrm{m\,s^{-1}}$ and $400\,\mathrm{m\,s^{-1}}$ (for $\tau_\mathrm{i} = 0.0025, 1, 3$) driven by an average normal curvature of about $0.16\,\mathrm{m^{-1}}$. This lets the filament propagate a distance much smaller than its perpendicular size $\delta_\perp$. The weak curvature is not able to drive significant $\mathbf{E} \times \mathbf{B}$ advection. The high variation of the curvature along the field line reduces the propagation further compared to the same simulation with the average

curvature of W7-X. This is consistent with the findings from the simulations with average drive and sinusoidal variation in section 4.

7. Summary and discussion

In this paper, the `hermes-2` model equations are solved using the `BOUT++` framework to investigate the coherence of filaments experiencing a parallel varying curvature drive.

For a constant curvature, the charge accumulation is even along the magnetic field line. A parallel varying curvature leads to a varying charge separation causing differential $\mathbf{E}\times\mathbf{B}$ advection along the field line. The parallel current sets in to reduce the inhomogeneous polarization. If the parallel current flattens the parallel potential gradient fast enough, the filament stays coherent along the field line. Otherwise, the differential $\mathbf{E}\times\mathbf{B}$ advection rips the filament apart into separate structures. The parallel displacement after one advection time $\tau_B = \delta_\perp/v_b$ between the point of lowest and the point of highest curvature is chosen as a measure of filament coherence.

The evolution of the parallel current is governed by parallel Ohm's law with the main control parameters being collisionality ν and the electron plasma beta β_e governing the ohmic resistance and the inductance terms. Normalized using the blob correspondence principle ν' and β_e' control the propagation time of the parallel current and determine the parallel displacement of different parallel parts of the filament. High ν' and β_e' decrease the propagation of the parallel current $j_\parallel$ against the perpendicular advection time of the blob allowing for differential displacement.

In individual scans of β_e' and ν', while the respective other parameter is negligible, the simulations have shown, that these parameters govern the normalized displacement $\Delta/\delta_\perp$. The parallel maximum displacement is found to be $\Delta/\delta_\perp = 2.67$. These results are compatible with previous work on the coherence of filaments in W7-X [17]. There, an increase in temperature has been found to increase filament coherence. As these simulations were dominated by collisions (cold, pellet-relevant conditions) an increase in temperature primarily decreases the collisionality which decreases the parallel displacement. The electron plasma beta is small.

Simulations with a sinusoidal curvature variation along the field line show significant displacement for sufficiently high values of $(\nu' + \beta_\mathrm{e}')$, exceeding the perpendicular blob size $\delta_\perp$. Deviations from the scaling $\Delta/\delta_\perp \sim (\nu' + \beta_\mathrm{e}')j_\parallel$ arise from the influence of the parallel pressure gradient $\partial_\parallel p_\mathrm{e} \sim 1/L_\parallel p_\mathrm{e}$. Its influence is increased for smaller connection lengths and it acts against the ohmic and inductive resistance terms. Therefore, simulations with similar values of $(\nu' + \beta_\mathrm{e}')$ show larger displacements for higher parallel connection lengths.

A sinusoidal curvature with an additional constant curvature drive is shown to decrease the filament velocity compared to the homogeneous curvature case if the amplitude of the variation is of a similar magnitude as the average drive. A large displacement leads to parallel flows driven by parallel pressure gradients $\partial_\parallel p_\mathrm{e}$. This decreases the amplitude of the perpendicular pressure perturbation reducing the drive of filament motion. For a density of $10^{19}\mathrm{m}^{-3}$ and a temperature of 100 eV which corresponds to comparatively high $(\nu' + \beta_\mathrm{e}')$, the filament velocity is reduced to $\approx$25% of the unperturbed case for a curvature variation four times higher than the average curvature.

Simulations of filaments in a circular tokamak and simulations of a field line from W7-X in areas relevant for a future diagnostic show displacements compatible with the previously motivated parameter dependencies. The displacement along the field line follows the curvature profile in the radial and binormal directions. Simulations with blob and background temperature and density inputs from AUG measurements show a small radial displacement of 0.34. This is compatible with the circular tokamak results as the pressure perturbations in the tokamak simulations are smaller.

The W7-X-like curvature shows a strong rippling of the curvature profile. The normalized displacement follows the curvature pattern for low ion temperatures demonstrating the strong correlation of curvature and filament displacement. This results in the normalized displacement exceeding one perpendicular blob size at the most prominent curvature feature in the hot ion $\tau_\mathrm{i} = 3$ case. This fits the displacement scaling as the curvature fall-off length and the pressure perturbations are lower.

The strong variation decreases the average filament velocity to only between 100 m s^{-1} and 400 m s^{-1}. This is in agreement with recent experimental and numerical findings [15] which show that filaments in W7-X are approximately bound to their initial flux surface and do not perform ballistic motion or turbulence spreading in the SOL. The effects of inductance and collisionality on the propagation of filaments should not play a big role in current stellarator experiments but could become influential for experiments with higher collisionality and or electron plasma beta in the SOL.

This work, like previous work in [16] and [17], considers one specific aspect of filament dynamics in stellarators—the non-uniform curvature—to investigate the physical mechanisms at play. The logical next step, which is pursued by the `BSTING` project [29], is to perform global simulations of stellarator edge and SOL turbulence.

Data availability statement

The data cannot be made publicly available upon publication because no suitable repository exists for hosting data in this field of study. The data that support the findings of this study are available upon reasonable request from the authors.

Acknowledgments

This work has been carried out within the framework of the EUROfusion Consortium, funded by the European Union via the Euratom Research and Training Programme (Grant Agreement No 101052200 - EUROfusion). Views and opinions expressed are however those of the author(s) only and do not necessarily reflect those of the European Union or the

European Commission. Neither the European Union nor the European Commission can be held responsible for them.

ORCID iDs

P Huslage https://orcid.org/0000-0002-2898-0413
G Birkenmeier https://orcid.org/0000-0001-7508-3646
B Shanahan https://orcid.org/0000-0002-8766-8542
C Killer https://orcid.org/0000-0001-7747-3066

References

[1] D'Ippolito D A, Myra J R and Zweben S J 2011 Convective transport by intermittent blob-filaments: comparison of theory and experiment *Phys. Plasmas* **18** 060501
[2] Seidl J, Jirakova K, Adamek J, Grover O, Horacek J, Hron M and Vondracek P 2018 Fluctuations in the scrape-off layer and edge plasma of the COMPASS tokamak *45th EPS Conf. on Plasma Physics*
[3] Kočan M, Gennrich F P, Kendl A and Müller H W 2012 Ion temperature fluctuations in the ASDEX Upgrade scrape-off layer *Plasma Phys. Control. Fusion* **54** 085009
[4] Carralero D, Birkenmeier G, Müller H W, Manz P, deMarne P, Müller S H, Reimold F, Stroth U, Wischmeier M and Wolfrum E 2014 An experimental investigation of the high density transition of the scrape-off layer transport in ASDEX Upgrade *Nucl. Fusion* **54** 123005
[5] Birkenmeier G *et al* 2015 Filament transport, warm ions and erosion in ASDEX Upgrade L-modes *Nucl. Fusion* **55** 033018
[6] Zweben S J, Boedo J A, Grulke O, Hidalgo C, LaBombard B, Maqueda R J, Scarin P and Terry J L 2007 Edge turbulence measurements in toroidal fusion devices *Plasma Phys. Control. Fusion* **49** S1
[7] Carralero D, Calvo I, Shoji M, Carreras B A, Ida K, Ohdachi S, Sakakibara S, Yamada H and Hidalgo C 2011 Influence of β on the self-similarity properties of LHD edge fluctuations *Plasma Phys. Control. Fusion* **53** 095010
[8] Killer C, Narbutt Y and Grulke O (the W7-X Team) 2021 Turbulent transport in the scrape-off layer of Wendelstein 7-X *Nucl. Fusion* **61** 096038
[9] Grulke O, Klinger T, Endler M and Piel A 2001 Analysis of large-scale fluctuation structures in the scrape-off layer of the Wendelstein 7-AS stellarator *Phys. Plasmas* **8** 5171–80
[10] Endler M, Giannone L, McCormick K, Niedermeyer H, Rudyj A, Theimer G, Tsois N and Zoletnik S (The ASDEX Team1 and the W7-AS Team) 1995 Turbulence in the SOL of ASDEX and W7-AS *Phys. Scr.* **51** 610–6
[11] Fuchert G 2013 Dynamics and structure analysis of coherent turbulent structures at the boundary of toroidally confined plasmas *Doctoral Thesis* Universität Stuttgart (available at: http://elib.uni-stuttgart.de/handle/11682/2349)
[12] Bleuel J, Endler M, Niedermeyer H, Schubert M and Thomsen H (W7-AS) 2002 The spatial structure of edge fluctuations in the Wendelstein 7-AS stellarator *New J. Phys.* **4** 338
[13] Schubert M, Endler M and Thomsen H 2007 Spatiotemporal temperature fluctuation measurements by means of a fast swept Langmuir probe array *Rev. Sci. Instrum.* **78** 053505
[14] Tanaka K *et al* 2006 Experimental study of particle transport and density fluctuations in LHD *Nucl. Fusion* **46** 110–22
[15] Killer C, Shanahan B, Grulke O, Endler M, Hammond K and Rudischhauser L 2020 Plasma filaments in the scrape-off layer of Wendelstein 7-X *Plasma Phys. Control. Fusion* **62** 085003
[16] Shanahan B and Huslage P 2020 Filament simulations in regions of highly-varying parallel connection length *J. Plasma Phys.* **86** 905860314
[17] Shanahan B, Dudson B and Hill P 2018 The effects of non-uniform drive on plasma filaments *J. Phys.: Conf. Ser.* **1125** 012018
[18] Dudson B D and Leddy J 2017 Hermes: global plasma edge fluid turbulence simulations *Plasma Phys. Control. Fusion* **59** 054010
[19] Dudson B, Muhammed H, Shanahan B and Omotani J Hermes-2 Git Repo (available at: https://github.com/bendudson/hermes-2)
[20] Simakov A N and Catto P J 2003 Drift-ordered fluid equations for field-aligned modes in low-β collisional plasma with equilibrium pressure pedestals *Phys. Plasmas* **10** 4744–57
[21] Gray D and Giorgini A 1976 The validity of the boussinesq approximation for liquids and gases *Int. J. Heat Mass Transfer* **19** 545–51
[22] Braginski S 1965 Transport processes in a plasma *Reviews of Plasma Physics* vol 1 ed M A Leontovich (Consultants Bureau) pp 205–311
[23] Schneider R, Bonnin X, Borrass K, Coster D P, Kastelewicz H, Reiter D, Rozhansky V A and Braams B J 2006 Plasma edge physics with B2-Eirene *Contrib. Plasma Phys.* **46** 3–191
[24] Madsen J, Naulin V, Nielsen A H and Rasmussen J J 2016 Collisional transport across the magnetic field in drift-fluid models *Phys. Plasmas* **23** 032306
[25] Krasheninnikov S I, D'ippolito D A and Myra J R 2008 Recent theoretical progress in understanding coherent structures in edge and SOL turbulence *J. Plasma Phys.* **74** 679–717
[26] Garcia O E, Bian N H and Fundamenski W 2006 Radial interchange motions of plasma filaments *Phys. Plasmas* **13** 082309
[27] Helander P 2018 Corrigendum: theory of plasma confinement in non-axisymmetric magnetic fields (2014 Rep. Prog. Phys. 77 087001) *Rep. Prog. Phys.* **81** 099501
[28] Nasim M H, Rafiq T and Persson M 2004 Geometrical effects on drift wave stability in low shear stellarator plasmas *Plasma Phys. Control. Fusion* **46** 193
[29] Shanahan B, Dudson B and Hill P 2019 Fluid simulations of plasma filaments in stellarator geometries with BSTING *Plasma Phys. Control. Fusion* **61** 025007
[30] Lewandowski J L V and Persson M 1995 Local magnetic shear in tokamak plasmas *Plasma Phys. Control. Fusion* **37** 1199–205
[31] Terry J, Baek S G and Ballinger S 2018 Design of a gas-puff imaging diagnostic for W7-X *60th Annual Meeting of the APS Division of Plasma Physics* vol 63 p 11
[32] Bozhenkov S A, Geiger J, Grahl M, Kißlinger J, Werner A and Wolf R C 2013 Service oriented architecture for scientific analysis at W7-X. An example of a field line tracer *Fusion Eng. Des.* **88** 2997–3006